Geophysical Research Letters

RESEARCH LETTER
10.1029/2025GL114885

Microphysics Dominates Sub-Cloud Rain Evaporation in Trade Cumuli Over Barbados

M. Sarkar[1,2], R. Vogel[3], and Y. Zheng[1,2]

[1]Institute of Climate and Atmospheric Science, University of Houston, Houston, TX, USA, [2]Department of Earth and Atmospheric Sciences, University of Houston, Houston, TX, USA, [3]Universitat Hamburg, Hamburg, Germany

Key Points:

- Cloud base microphysical properties are critical in assessing the rain evaporation characteristics
- The evaporated fraction depends strongly on the raindrop size, and the flux depends primarily on the drop concentration
- Thermodynamic processes show smaller control on rain evaporation in trade cumulus

Supporting Information:

Supporting Information may be found in the online version of this article.

Correspondence to:

M. Sarkar and Y. Zheng,
msarkar2@uh.edu;
yzheng29@central.uh.edu

Citation:

Sarkar, M., Vogel, R., & Zheng, Y. (2025). Microphysics dominates sub-cloud rain evaporation in trade cumuli over Barbados. *Geophysical Research Letters*, *52*, e2025GL114885. https://doi.org/10.1029/2025GL114885

Received 22 JAN 2025
Accepted 6 OCT 2025

Author Contributions:

Conceptualization: M. Sarkar
Data curation: R. Vogel
Formal analysis: M. Sarkar, Y. Zheng
Funding acquisition: Y. Zheng
Investigation: M. Sarkar, R. Vogel
Methodology: M. Sarkar
Project administration: M. Sarkar, Y. Zheng
Resources: R. Vogel, Y. Zheng
Software: M. Sarkar
Supervision: Y. Zheng
Validation: M. Sarkar, R. Vogel, Y. Zheng
Visualization: M. Sarkar, R. Vogel, Y. Zheng
Writing – original draft: M. Sarkar
Writing – review & editing: M. Sarkar, R. Vogel, Y. Zheng

Abstract This study investigates the microphysical and thermodynamic influences on North Atlantic trade-cumulus rain evaporation in the sub-cloud layer over Barbados from January to November 2020. Using radar observations and a 1-D model, the results reveal that microphysical properties, namely geometric mean diameter (D_g) and raindrop concentration, primarily control evaporation processes under conditions of limited thermodynamic variability. Thermodynamic factors like cloud base height and relative humidity exert a smaller influence due to their narrow observed ranges. Small D_g leads to rapid increases in rain evaporation fraction (REF), as small drops evaporate completely, while larger D_g yields slower, more gradual REF changes. Frequent weak-rain cases reduce the mean evaporation flux, whereas infrequent intense-rain events substantially enhance it. These findings highlight the pivotal role of microphysical variability in shaping sub-cloud evaporation in this trade cumulus regime, while thermodynamic effects may be more important in other environments.

Plain Language Summary Rain evaporation reduces surface rainfall and can trigger downdrafts and cold pools, influencing cloudiness. This study examines how raindrop microphysical and thermodynamic factors, like cloud base height and surface relative humidity, influence rain evaporation over Barbados from January to November 2020. Raindrop properties at cloud base govern sub-cloud evaporation, while thermodynamics factors matter less due to their limited variability. Smaller drops evaporate completely, increasing evaporation fraction, while large drops reach the surface. Overall, microphysics primarily drives rain evaporation processes.

1. Introduction

Rain evaporation in the sub-cloud layer significantly influences the moisture and heat budgets in tropical and sub-tropical cumulus environments. It plays a critical role in cooling and moistening the sub-cloud layer, leading to cold pool formation and impacting the mesoscale clustering of clouds in the trade cumulus regime (Jensen et al., 2000; Radtke et al., 2023; Seifert & Heus, 2013; Tompkins, 2001). Additionally, rain evaporation recycles moisture and feeds into large-scale circulations (Stevens, 2005; Worden et al., 2007). Recent studies indicate that 50% of the water vapor contributing to moist patches in the tropical boundary layer, especially near the surface, originates from rain evaporation (Torri & Kuang, 2016). This highlights the importance of characterizing long-term rain evaporation and understanding the underlying factors.

However, analyzing rain evaporation remains challenging due to the limited availability of high-resolution, long-term rain observational data sets in marine environments. Past studies suggest the role of microphysical and thermodynamic processes in the boundary layer on the rain evaporation processes. For example, a water vapor isotope satellite-based study over six months estimated 20%–50% of rain evaporates in tropical convective cloud environments (Worden et al., 2007). Similarly, Naumann and Seifert (2016) showed the role of large raindrops in contributing to surface precipitation in large-eddy simulations of the Rain in the shallow cumulus over the ocean (RICO) campaign cases. More recently, Sarkar et al. (2023a, 2023b) showed that 63% of rain mass evaporates in the sub-cloud layer using aircraft field campaign observations over 4 days in the trade cumulus regime in the north Atlantic Ocean, highlighting significant dependencies on microphysical conditions. While these studies provide valuable insights, their limited timeframes make it difficult to draw climatic inferences.

Furthermore, microphysical schemes in models like community atmosphere model version 5 (CAM5), which underpin global climate models such as DOE Energy Exascale Earth System (E3SM) and NSF Community Earth System Model, lack detailed rain evaporation processes and rely on bulk thermodynamic conditions (e.g., Conley

10.1029/2025GL114885

et al., 2012; Sundqvist et al., 1989). This could potentially impact the performance of shallow rain schemes in global models. For example, Zheng et al. (2020) showed that E3SMv1 underestimated rain evaporation rates in the marine boundary layer while also simulating the maximum rain evaporation closer to the surface, as compared to ARM observations. Similarly, Fletcher et al. (2014) showed overestimated precipitation in shallow convective and stratiform environments based on the single-column configuration of the NCEP-GFS model, which is likely also linked to an underestimation of rain evaporation. These shortcomings could be addressed through more detailed, long-term observational analyses with improved microphysical characterization.

In this study, we utilize ground-based radar, lidar and surface in situ observations January–November 2020 at the Barbados Cloud Observatory (BCO, 13.1939°N, 59.5432°W, Stevens et al., 2016) in the north Atlantic Ocean. Barbados has been established as an anchor point for studying trade-wind cumulus because its cloud and precipitation characteristics are broadly representative of the wider trades. Brueck et al. (2015) concluded that conditions upstream of Barbados are typical of trade-wind regimes, with seasonal variability tied to the ITCZ. Medeiros and Nuijens (2016) likewise show that clouds in Barbados are similar to those across the trade wind regions, implying that observational findings from the Barbados Clouds Observatory (BCO) are relevant to clouds across the tropics. Stevens et al. (2016) further emphasized that seasonal shifts in cloudiness at the BCO appear representative of processes in the broader trades. These findings justify the extrapolation of our Barbados-based results to the North Atlantic trade-wind regime.

We also incorporate aircraft-based in situ rain microphysical observations from the ElUcidating the RolE of Clouds-Circulation Coupling in ClimAte (EUREC^{4}A) field campaign conducted near Barbados January–February 2020 to constrain the microphysical retrievals (Bony et al., 2022; Stevens et al., 2021). By combining these observations with a one-dimensional bin-based rain evaporation model, we extend previous short-term analyses by isolating the effects of microphysical and thermodynamic processes on sub-cloud rain evaporation over an 11-month period. The inferred results are tested in both weak and intense rain regimes, as well as small and large raindrop regimes, for a comprehensive characterization. An additional empirically driven model, the sedimentation-evaporation model (Comstock et al., 2004), is used to obtain bulk rain evaporation. Details of the observations and models are provided in Section 2, followed by the results in Section 3 and conclusions and discussion in Section 4.

2. Data and Methodology

2.1. Barbados Clouds Observatory (BCO) and ATR/EUREC^{4}A Campaign Observations

The BCO is in the North Atlantic trades at Deebles point, about 30 m from the shore and at 17 m elevation on a cliff to protect the site from wave breaks (Stevens et al., 2016). Barbados Clouds Observatory provides a rare long-term, high-frequency record of radar, lidar and in situ observations, making it exceptionally valuable for quantifying rain evaporation processes in this typically under-sampled marine environment (see Text S1 in Supporting Information S1 for instrument details).

To complement the ground-based BCO record, in situ rain microphysical measurements were obtained from the French SAFIRE ATR42 research aircraft (ATR) during 19 flights over the western tropical Atlantic near Barbados (25 January–13 February 2020) as a part of the EUREC^{4}A campaign (Bony et al., 2022, details in Text S1 in Supporting Information S1). The unique combination of BCO's continuous observations with EUREC^{4}A's detailed microphysical data ensures robust retrievals and analysis of rain evaporation in the North Atlantic trades.

2.2. Radar-Retrieval Methodology

We use 1-Hz raindrop size distribution (RSD) from ATR to generate in situ equivalent radar reflectivity (Z)-binned look-up table of microphysical parameters. For each 11 Z bins (−20 to 45 dBZ), mean RSDs are fit with a three-parameter lognormal function to derive geometric mean diameter (D_g), width ($\boldsymbol{\sigma}$) and total concentration (N_0) using the method of moments (Equations S2–S5 and Figure S2 in Supporting Information S1). Lognormal fits consistently outperform exponential fits, especially at larger drop sizes. The robustness of the lognormal fits is quantified by calculating the RMSE and correlation coefficient (r) between the fitted and observed RSD for each Z bin (Table S2 in Supporting Information S1).

At BCO, 15-min Ka-band radar Z and Doppler velocity (v_d) are used to retrieve D_g and N_0 profiles using a forward-modeling approach (Equations S8–S10 and Figure S1 in Supporting Information S1). D_g is retrieved by

10.1029/2025GL114885

matching modeled v_d to observed v_d using fixed $\boldsymbol{\sigma}$ values from the ATR-based lookup table. Given D_g and $\boldsymbol{\sigma}$, N_0 is then retrieved by minimizing the difference between modeled and observed Z. The main steps of the retrieval, associated instruments and representative uncertainties are summarized in Table S3 in Supporting Information S1. Monthly uncertainties are quantified by bootstrap resampling of raining samples.

$\boldsymbol{\sigma}$ shows low variability across reflectivity bins compared to D_g and N_0, supporting its use as a fixed parameter (Figure S3 in Supporting Information S1). The low variability of $\boldsymbol{\sigma}$ is quantitatively supported by coefficient of variation analysis. A Kruskal-Wallis test further confirms that $\boldsymbol{\sigma}$'s variability is significantly lower than that of D_g or N_0 ($p < 0.01$), which confirm that $\boldsymbol{\sigma}$ is substantially less variable than D_g or N_0 across all Z bins. This provides a rigorous justification for holding $\boldsymbol{\sigma}$ fixed in the retrieval. This simplification enables robust radar-based microphysical retrievals consistent with previous studies (Feingold & Levin, 1986; Sarkar et al., 2021). Median BCO-retrieved D_g and N_0 compare well with ATR-derived values across Z bins, validating the retrieval technique (Figure S6 and Table S1 in Supporting Information S1). We also tested robustness by constructing look-up tables for $\boldsymbol{\sigma}$ using independent ATR subsets (flights 1–13 vs. 14–19). The ATR-based D_g and N_0 from the two subsets have strong correlations ($r = 0.77$ and 0.99, respectively, Figure S7a–S7b in Supporting Information S1). The corresponding rain evaporation fraction (REF) and F_{eT} profiles also show negligible differences ($r > 0.9$, Figure S7c–S7d in Supporting Information S1). This confirms that the retrievals and model outputs are not sensitive to the ATR sampling.

2.3. Rain Evaporation Metrics

The 15-min microphysical lognormal parameters D_g and N_0 are retrieved from the BCO Z and v_d radar observations for all Ka-band radar samples between January and November. The retrieved D_g, N_0 are then used to compute the corresponding rain rates, R at 15-min time resoultion and 31.8 m vertical resolution between cloud base and the lowest usable radar range gate of 361.47 m. The vertical columns of R are further normalized with respect to altitude to remove the effect of cloud base variability throughout the study period. The normalized altitude z^* is calculated as $z^* = \frac{z - 361.47\ \mathrm{m}}{\mathrm{CBH} - 361.47\ \mathrm{m}}$, where z is the actual radar range gate altitude and 361.47 m is the lowest radar range gate used in this study. z^* is 0 at 361.47 m and 1 at cloud base and is calculated at (Δz^*=) 0.01 resolution. The raining columns are identified as vertical columns with cloud base rain rate (R_{cb}) exceeding 0.01 mm d^{-1}.

Two metrics are used to quantify rain evaporation using vertically retrieved normalized raining columns in the sub-cloud layer: REF and Rain evaporation flux (F_{eT}) (Equations 12–13 and Text S4 in Supporting Information S1). REF represents the fraction of rain mass that evaporates within the sub-cloud layer, offering insight into the efficiency of evaporation under varying rain conditions. It helps in quantifying what percent of rain mass contributes to boundary layer moisture versus surface precipitation. On the other hand, F_{eT} measures the total mass flux of evaporated rain, which is critical for assessing how much evaporated moisture enters the atmosphere, influencing large-scale thermodynamic processes. Both REF and F_{eT} will be used in this study to assess the influence of microphysical variability on rain evaporation.

2.4. Rain Evaporation Models

Two rain evaporation models are used to simulate the rain evaporation characteristics in this study, namely sedimentation-evaporation model (Comstock et al., 2004) and single column bin-resolved Lagrangian model (Sarkar et al., 2023a, 2023b), henceafter referred to as C04 and S23, respectively. The C04 model is a bulk exponential formulation that simulates rain evaporation below cloud base under steady-state conditions. It is initialized using R_{cb} and mean drop radius, and assumes no microphysical interactions or thermodynamic feedbacks. Its simplicity allows quick estimation of evaporation profiles and has been used in field campaign and satellite retrievals.

The S23 model is a bin-resolved Lagrangian model that tracks raindrop evolution as it falls through the sub-cloud layer. It calculates vertical variations in drop size, temperature and evaporation using numerical integration at 1-m vertical resolution, assuming steady-state conditions. Without collision-coalescence, turbulence, wind shear or feedback from evaporated rain on the background moisture. The model is initialized with cloud base microphsycial retrievals, RH_{sf} and cloud base height (CBH),with RH assumed to decrease linearly to surface. S23 provides detailed vertical profiles of rain rate, REF and F_e. Full details of both models are provided in Text S5 in Supporting Information S1.

3. Results

3.1. Seasonal Meteorological, Microphysical, and Rain Evolution

Figure 1 presents the monthly variability of key parameters relevant to sub-cloud rain evaporation, including surface relative humidity (RH_{sf}), CBH, radar-derived microphysical properties D_g and N_0 at cloud base, radar-derived rain rates at cloud base and surface, and rain frequency, computed only over raining samples, defined as when $R_{cb} > 0.01$ mm d^{-1}. This ensures that all variables shown correspond to active precipitating conditions. The rain frequency in each month is computed as the ratio of 15-min cloud base samples with $R_{cb} > 0.01$ mm d^{-1} to the total number of 15-min samples in that month.

Both RH_{sf} and CBH (Figure 1a) show seasonality with RH_{sf} lowest in March and recovering in summer and fall, whereas CBH peaking in spring and lowest in fall, consistent with climatological patterns and the annual cycle of boundary layer moistening (e.g., Brueck et al., 2015; Chang & Oey, 2013; Leon et al., 2008). Overall, monthly RH_{sf} varies within 75%–85%, and CBH remains within 700–900 m through the year.

The monthly mean rain rates at both cloud base (R_{cb}) and surface (R_{sf}) show the highest radar-based rain rates in January, driven by an intense rain event between January 22–25, with peak rates up to 100 mm hr^{-1}. This event aligns with the classic Fish pattern, like in Vogel et al. (2021). Annual mean rain rate shows a significant decrease from cloud base (3.3 ± 7.8 mm hr^{-1}) to surface (1.8 ± 4.7 mm hr^{-1}) (Figures 1b and 1c), reflecting the rain mass evaporating in the sub-cloud layer. Annual mean rain sample frequency also decreases from 35% to 24%, further highlighting sub-cloud evaporation processes. Comparatively, the WXT-based rain frequency at the surface remains below 15% throughout the year, which potentially is due to larger sampling threshold of the instrument.

Radar-retrieved microphysical properties at cloud base show marked seasonality (Figure 1d). $D_{g,cb}$ is lowest in winter and spring, rising through late summer and fall from 0.25 to 0.35 mm. $N_{0,cb}$ follows an inverse pattern, with maximum values early in the year and vice versa. These trends reflect changes in RSD with larger but fewer drops in the later months, which could impact the rain evaporation potential.

3.2. Seasonal Evolution of Radar-Retrieved and Modeled Rain Evaporation Characteristics

The S23 model R_{sf} (Figure 1b, green) demonstrates reasonable agreement with radar-retrieved rain characteristics, though notable biases emerge. R_{sf} is slightly underestimated by S23 model, especially in March–July, indicating overestimated evaporation. This is confirmed by the higher S23-based REF and slightly elevated F_{eT} compared to radar (Figures 1e and 1f). However, the interquartile ranges of both REF and F_{eT} show good overlap for most of the year, especially for F_{eT}. Their monthly shapes are also well captured by S23, indicating its ability to simulate rain evaporation. Section 3.5 will further examine the S23 and radar-retrieal biases.

In contrast to S23, the C04 model, which is initialized using the radar-retrieved R_{cb}, highly overestimates R_{sf}, and hence underestimates both REF and F_{eT}, especially REF (yellow). The high C04-based R_{sf}, which is almost equal to R_{cb}, suggest negligible rain evaporation. Despite the underestimated magnitudes, C04 can simulate the shape of the monthly variations of REF and F_{eT} quite well, suggesting that improving the empirical formulations in the model may improve its performance in rain evaporation studies. Due to the overall better performance of S23 in simulating the F_{eT} and REF structures, the sensitivity tests are based only on the S23 model.

Notably, the 15-min year-long RSD is predominantly composed of small $D_{g,cb}$ (Figure S4 in Supporting Information S1), which produce high REF but low F_{eT}, resulting in annual high median REF and low median F_{eT}. However, the less frequent larger $D_{g,cb}$ cases skew the annual mean to lower REF and higher F_{eT} values. This separation between mean and median highlights the need to consider both frequent weak-rain and rare intense-rain regimes when interpreting climatological statistics.

3.3. Dependence of REF and F_{eT} on Microphysics

To quantify the relative roles of microphysics and thermodynamics in driving monthly variations of F_{eT} and REF, we perform four sensitivity tests (Figure 2). In each test, one parameter among $D_{g,cb}$, $N_{0,cb}$, CBH or RH_{sf}, is allowed to follow its observed monthly cycle, while the other three were fixed at their annual mean values ($N_{0,cb}$, $D_{g,cb}$, CBH and RH_{sf} of 10^3 m^{-3}, 0.28 mm, 800 m and 80%, respectively). This setup allows us to directly assess the contribution of each parameter to rain evaporation. Smaller perturbations (test - control) indicate a greater influence of the parameter in driving seasonal variations.

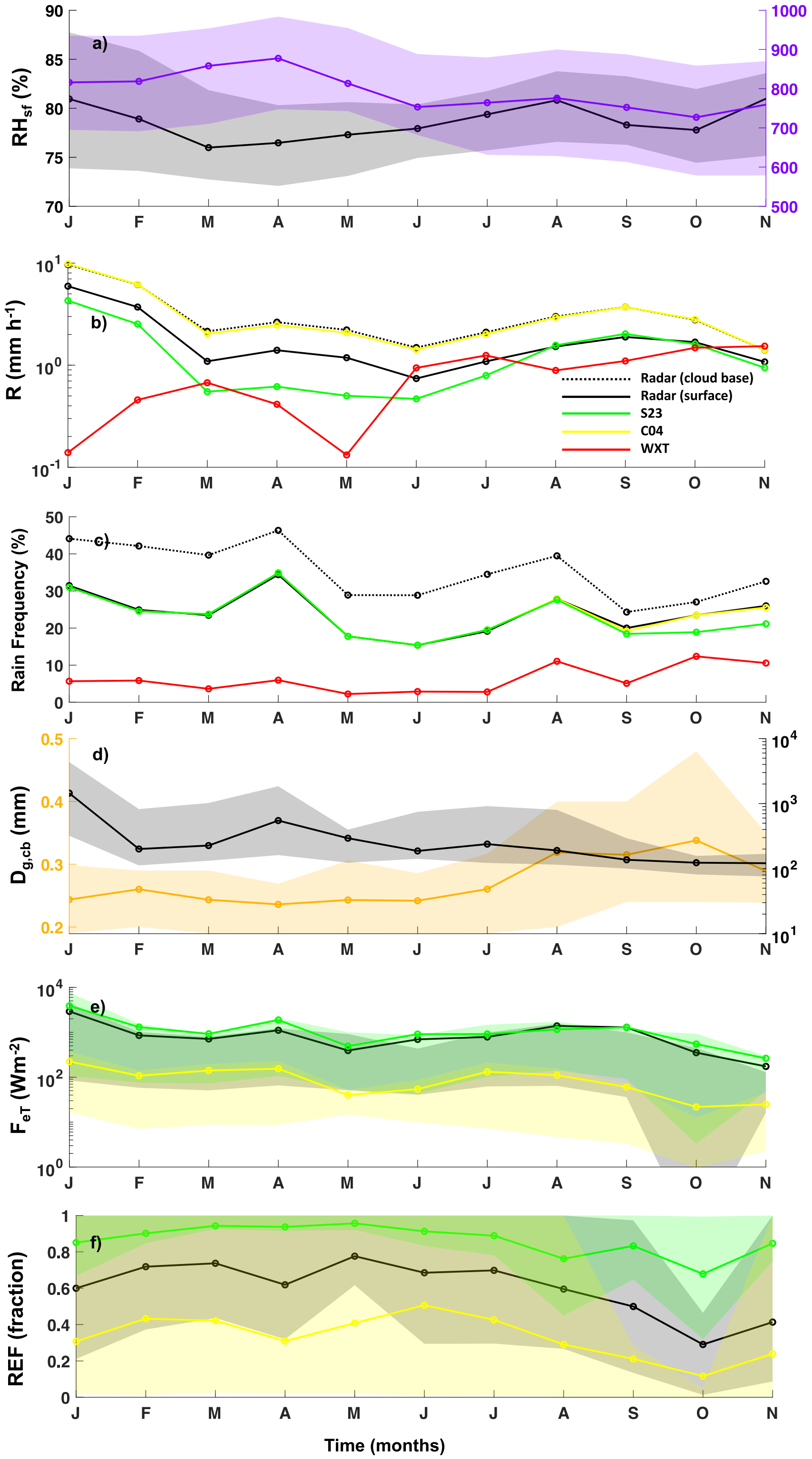

Figure 1. (a) Monthly mean RH_{sf} (left black) and cloud base height (right purple), averaged over raining samples ($R_{cb} > 0.01$ mm d^{-1}). (b) Rain rates at cloud base (dotted black) and surface (solid black) from radar retrievals, S23 (green) and C04 (yellow) models and WXT observations (red). (c) Monthly rain frequency (% of cloud-base samples with $R_{cb} > 0.01$ mm d^{-1}). (d) Monthly mean radar-retrieved $D_{g,cb}$ (left orange) and $N_{0,cb}$ (right black) with 25–75th percentiles. (e) and (f) Monthly mean F_{eT} and rain evaporation fraction from radar, S23 and C04 with colors following legend in (b). Shaded bands denote 25th–75th percentile ranges.

10.1029/2025GL114885

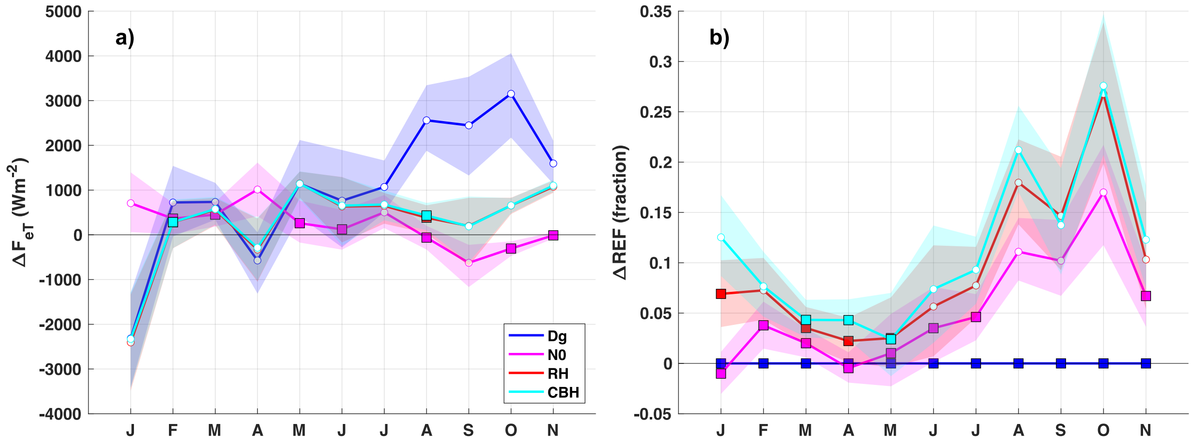

Figure 2. Monthly perturbations (test-control) in (a) F_{eT} and (b) rain evaporation fraction from S23 sensitivity runs, each allowing one parameter to freely vary ($N_{0,cb}$: magenta; $D_{g,cb}$: blue; CBH: cyan; RH_{sf}: red; control: green), while holding other parameters fixed at their annual mean values. The smaller the perturbation is, the more determinant the variable drives the seasonal variations. Shaded bands show 95% bootstrap confidence intervals; markers denote TOST equivalence outcomes with filled squares showing perturbations statistically equivalent to the control within tolerance margins ($p < 0.05$), while open circles denote non-equivalence.

REF is a strong function of $D_{g,cb}$ as shown by the complete overlap between the control run (green) and the "$D_{g,cb}$ varying" run (blue) in Figure S8 in Supporting Information S1 and Figure 2b. In contrast, varying only $N_{0,cb}$ (magenta) produces minimal REF variability, and perturbations in CBH (cyan) or RH_{sf} (red) fail to reproduce the seasonal cycle. This indicates that, within the limited range of CBH and RH_{sf} sampled at BCO, $D_{g,cb}$ is both necessary and sufficient to predict REF.

The negligible effect of $N_{0,cb}$ arises from cancellation of N_0 terms between cloud base and surface in the REF (Equations S12 in Supporting Information S1), since $N_{0,sf} << N_{0,cb}$. Because most cloud-base RSDs are dominated by small $D_{g,cb}$ cases, drops tend to evaporate completely, REF ≈ 1 regardless of $N_{0,cb}$. Similarly, the relatively narrow observed ranges of RH_{sf} and CBH are likely too small to strongly affect REF. In regions of larger thermodynamic variability, such as convective systems or stratocumulus to cumulus transition regimes, thermodynamic influences on REF could be more substantial.

In contrast to REF, F_{eT} is dominated by $N_{0,cb}$ (magenta, Figure 2a). Perturbations in $D_{g,cb}$, RH_{sf} and CBH (red, cyan) exert secondary effects. Varying only $N_{0,cb}$ reproduces most of the control-run F_{eT} shape and magnitude. RH_{sf} and CBH perturbations capture modest control effects, while $D_{g,cb}$-only runs capture little variability, especially in fall months, when $D_{g,cb}$ is very high (Figure 1d). Because F_{eT} is largely set by $N_{0,cb}$, which also determines cloud-base rain rate, R_{cb} remains a useful bulk predictor of F_{eT}, consistent with their strong correlation in Figures 1b and 1e. The robustness of these findings is supported by the 95% bootstrap confidence intervals and TOST markers in Figure 2, which confirm that the identified parameter influences are statistically robust rather than artifacts of sampling noise.

3.4. Microphysical Influence on Radar-Retrieved Vertical REF and F_e Distributions

The influence of microphysical properties on the vertical structures of REF and F_e are shown in Figure 3 for radar-retrieval (left) and model (right). F_e is the flux resolved at each z*. For small $D_{g,cb}$ (<0.3 mm), REF often approaches 1 near the surface indicating near-complete evaporation of all its rain mass in the sub-cloud layer (Figure 3a). Some of this evaporation occurs very close to the cloud base, while others somewhere in the mid-way. This shallow and rapid evaporation in small $D_{g,cb}$ can lead to high REF near cloud base.

In contrast, larger $D_{g,cb}$ cases show slower increase in REF toward the surface, as larger drops are more resistant to evaporation and tend to reach the surface due to their higher terminal velocities. These contrasting REF profiles highlight that the efficiency and depth of rain evaporation are strongly modulated by cloud-base drop sizes.

As $N_{0,cb}$ increases (Figure 3e), F_e increases at all heights, which also raises the integrated flux F_{eT}. Profiles with low to mid $N_{0,cb}$ are variable, with some columns evaporating completely before reaching the surface, likely when drops are small. At high $N_{0,cb}$, F_e is consistently strong and surface-reaching, giving the highest F_{eT}. In contrast, $D_{g,cb}$ mainly affects the vertical shape of F_e (Figure 3c). Small drops (<0.25 mm) evaporate quickly near cloud

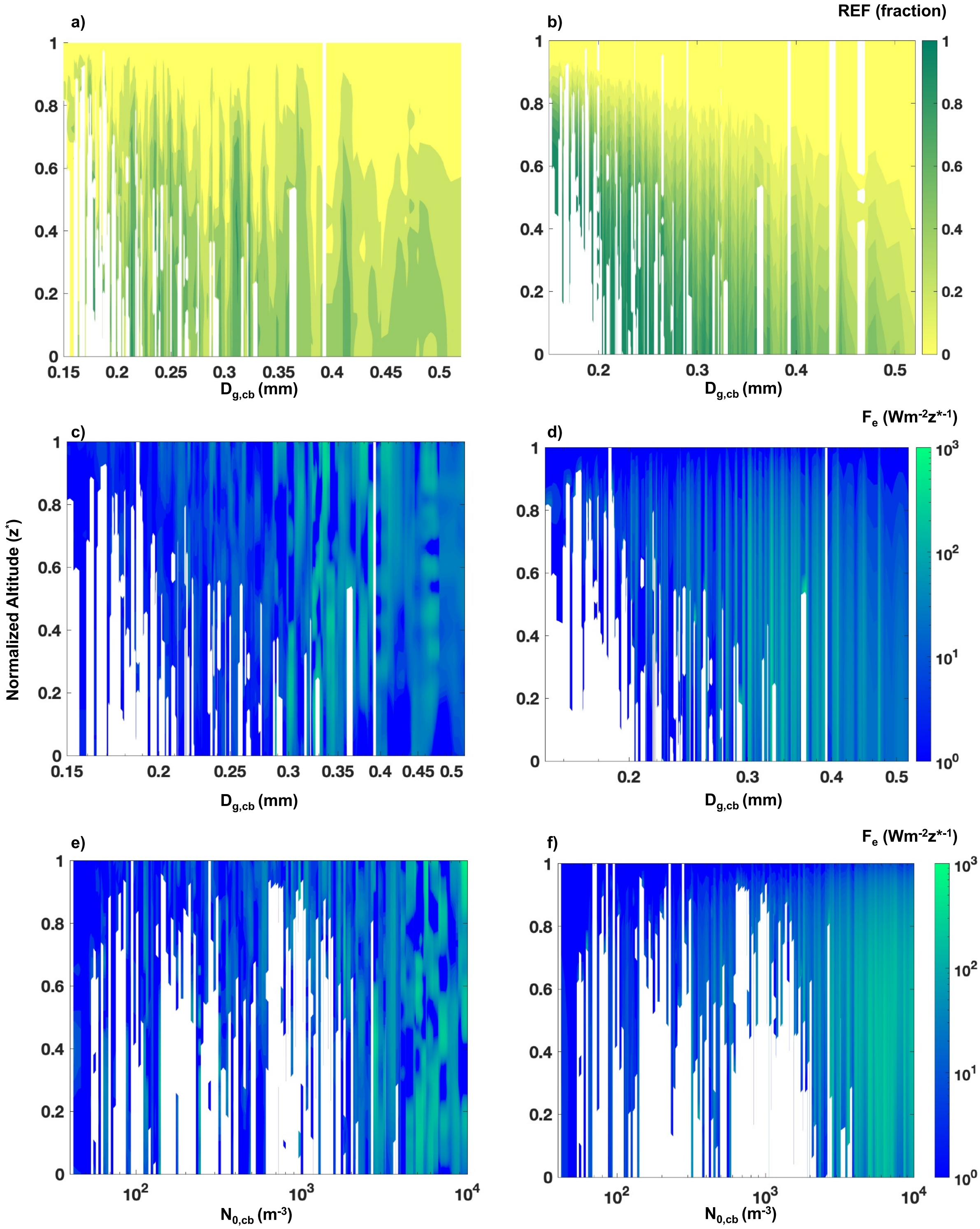

Figure 3. Vertical structure of rain evaporation comparing observations (left) with S23 outputs (right). All panels plot normalized height z^* on the y-axis versus a control parameter on x-axis with rain evaporation fraction (fraction) against $D_{g,cb}$ (a–b), F_e (Wm^{-2} z^{*-1}) against $D_{g,cb}$ (c–d) and F_e against $N_{0,cb}$ (e–f).

base, producing top-heavy profiles and frequent complete evaporation. As $D_{g,cb}$ increases, more rain survives to the surface and F_e grows through the column. For the largest drops, F_e remains strong but the increase levels off, suggesting F_{eT} is not as strongly tied to $D_{g,cb}$ as it is to $N_{0,cb}$ (as also confirmed in Figure 2). Together these results show that $N_{0,cb}$ sets the overall magnitude of F_{eT}, while $D_{g,cb}$ determines how evaporation is distributed with height.

3.5. Model Performance in Different Microphysical Regimes

The S23 model captures the overall vertical structure of REF and F_e reasonably well. Modeled REF increases smoothly with height, consistent with observations. Likewise, F_e magnitudes below $z^* < 0.9$ are comparable to observations, suggesting that the model reproduces bulk rain evaporation effectively. Differences arise, however, in the detailed vertical distribution.

For small-$D_{g,cb}$ regimes, the model tends to overestimate REF, with near-surface values approaching unity more often than observed, suggesting more complete evaporation of small drops in S23 than in radar retrievals. In large-$D_{g,cb}$ regimes, the model produces a bottom-heavy F_e profile, with reduced evaporation aloft and enhanced evaporation near the surface, whereas observations show a more vertically uniform structure. These patterns are attributed to small biases in modeled $D_{g,cb}$: a slight $D_{g,cb}$ overestimation near cloud base (mean bias = +0.008 mm) reduces F_e aloft, while a slight underestimation (mean bias = −0.005 mm) near the surface enhances evaporation and raises near-surface F_e and REF.

Despite these differences in vertical distribution, F_e remains in close agreement with observations, with an annual mean error of ∼30% and a strong correlation $r = 0.87$, reflecting its dependence on $N_{0,cb}$. By contrast, S23 overestimates REF in small drop regimes, but it remains reliable for assessments in large-drop regimes (annual mean error of ∼45%, $r = 0.73$). Together, these results highlight F_{eT} as a robust quantity of sub-cloud evaporation, with REF adding important insight into microphysical regime dependence.

4. Conclusions and Discussion

This study investigates sub-cloud rain evaporation in Barbados using 1-year radar retrievals, in situ microphysics from EUREC4A, and a bin-resolved 1-D model (S23). In this regime of limited thermodynamic variability with RH_{sf} of 75%–85% and CBH of 700–900 m, evaporation is governed primarily by cloud-base microphysics: $D_{g,cb}$ control REF, while $N_{0,cb}$ determines F_{eT}. Thermodynamic influences such as RH_{sf} and CBH are secondary. Previous work (e.g., Naumann & Seifert, 2016; Srivastava, 1985) emphasize microphysical and thermodynamic influences on sub-cloud layer. Our climatological analysis isolates these roles more clearly, showing that microphysics dominates in Barbados, with thermodynamics likely more important in regimes of greater variability, such as stratocumulus-to-cumulus transitions or continental convection.

Past campaigns in the trade-wind Atlantic have shown that sub-cloud rain evaporation is a key component of the boundary-layer moisture and energy budgets, with both its magnitude and variability governed primarily by rain microphysics. For example, RICO aircraft and radar observations demonstrated that evaporation losses below cloud base depend strongly on the microphysics: small-drop rain shafts undergo substantial evaporation, while large-drop regimes are more likely to sustain precipitation to the surface (Snodgrass et al., 2009). The RICO campaign reported an average latent heat flux from surface-reaching precipitation of approximately 63 W m^{-2}, within the ranges observed in ATOMIC/EUREC4A (15–352 W m^{-2}; Sarkar et al., 2023a, 2023b). In comparison, our year-long BCO record spans a broader climatological envelope (10–1,000 W m^{-2}), capturing both frequent weak-rain and rare intense-rain regimes, and further confirms that microphysical variability remains the dominant control on sub-cloud evaporation in the trade-wind regime.

Radar-retrieved and modeled profiles show contrasting behaviors across drop-size regimes. Small-$D_{g,cb}$ cases (∼75% of samples) evaporate rapidly and nearly completely, driving REF toward unity and producing top-heavy Fe profiles. Larger-$D_{g,cb}$ cases evaporate more gradually, yielding more uniform F_e and lower surface REF. Climatologically, frequent small-$D_{g,cb}$ events elevate median REF and depress median F_{eT}, while rare but intense large-$D_{g,cb}$ events lower REF (∼0.6) and substantially increase F_{eT}. This duality highlights the importance of resolving both frequent weak-rain and infrequent intense-rain regimes.

The S23 model captures FeT with high accuracy and reproduces seasonal REF variability, though it tends to overestimate REF for small drops and produce bottom-heavy F_e profiles for large drops, linked to vertical biases in retrieved D_g. Uncertainties could also stem from model assumptions. Like other 1-D rainshaft studies in the trades (De Szoeke et al., 2024; Niebaum, 2024; Snodgrass et al., 2009), S23 assumes a linear RH profile, useful for simplicity and comparability. We did not test alternative RH structures here, but note that future work should explore more non-linear humidity profiles and allow evaporation to feed back on background moisture. The model also neglects turbulence and wind shear, which can redistribute moisture; radar Doppler velocity is corrected by subtracting lidar-based vertical wind to isolate the raindrop terminal velocity, but this approach cannot fully account for shear-driven or turbulent motions. Microphysical interactions are excluded as well. Based on ATR/EUREC^{4}A data sets Niebaum (2024) indicate collision-coalescence contributes <10% to sub-cloud evaporation for rain rates below 3 mm hr^{-1}. This suggests that its omission might not be critical in the trades, though it may matter for heavier rain. Despite these limitations, S23 remains effective for estimating bulk sub-cloud evaporation and attributing its microphysical and thermodynamic controls.

The long-term radar data set developed here provides rare constraints on sub-cloud rain evaporation and its microphysical drivers. Our record resolves REF, F_e, and F_{eT} tied directly to cloud-base conditions. This benchmark can inform improved shallow-rain parameterizations in climate models. Together, these results establish a framework for linking microphysical variability to sub-cloud evaporation and for extending such analyses to other cloud regimes where thermodynamic influences may play a stronger role.

Conflict of Interest

The authors declare no conflicts of interest relevant to this study.

Data Availability Statement

The ATR/EUREC^{4}A RSD observations are available at Coutris (2021). The BCO radar, lidar and surface observations are available at https://observations.mpimet.mpg.de/repository/entry/show?entryid=9c71b050-43f6-40cc-9424-627161c71ade. The S23 model code is archived in Sarkar et al. (2023a).

Acknowledgments

MS and YZ work are supported by the University of Houston Presidential Frontier Faculty start-up fund and the DOE Early Career Grant (DE-SC0024185). RV acknowledges support from an ERC starting grant (ROTOR Grant Number 101116282). The authors thank the Tropical Cloud Observations group at Max Planck Institute for Meteorology for maintaining the BCO.

References

Achtert, P., Brooks, I. M., Brooks, B. J., Moat, B. I., Prytherch, J., Persson, P. O. G., & Tjernström, M. (2015). Measurement of wind profiles by motion-stabilised ship-borne Doppler lidar. *Atmospheric Measurement Techniques*, *8*(11), 4993–5007. https://doi.org/10.5194/amt-8-4993-2015

Bony, S., Lothon, M., Delanoë, J., Coutris, P., Etienne, J. C., Aemisegger, F., et al. (2022). EUREC4A observations from the SAFIRE ATR42 aircraft. *Earth System Science Data*, *14*(4), 2021–2064. https://doi.org/10.5194/essd-14-2021-2022

Brueck, M., Nuijens, L., & Stevens, B. (2015). On the seasonal and synoptic time-scale variability of the North Atlantic trade wind region and its low-level clouds. *Journal of the Atmospheric Sciences*, *72*(4), 1428–1446. https://doi.org/10.1175/jas-d-14-0054.1

Chang, Y. L., & Oey, L. Y. (2013). Coupled response of the trade wind, SST gradient, and SST in the Caribbean Sea, and the potential impact on Loop Current's interannual variability. *Journal of Physical Oceanography*, *43*(7), 1325–1344. https://doi.org/10.1175/jpo-d-12-0183.1

Comstock, K. K., Wood, R., Yuter, S. E., & Bretherton, C. S. (2004). Reflectivity and rain rate in and below drizzling stratocumulus. *Quarterly Journal of the Royal Meteorological Society: A journal of the atmospheric sciences, applied meteorology and physical oceanography*, *130*(603), 2891–2918. https://doi.org/10.1256/qj.03.187

Conley, A. J., Garcia, R., Kinnison, D., Lamarque, J. F., Marsh, D., Mills, M., et al. (2012). Description of the NCAR community atmosphere model (CAM 5.0). *NCAR technical note*, *3*.

Coutris, P. (2021). SAFIRE ATR42: PMA/Cloud composite dataset [dataset]. *Aeris*. https://doi.org/10.25326/237

de Szoeke, S. P., Sarkar, M., Quinones Melendez, E., Blossey, P. N., & Noone, D. (2024). A simple model for the evaporation of hydrometeors and their isotopes. *Journal of Geophysical Research: Atmospheres*, *129*(22), e2024JD041126. https://doi.org/10.1029/2024jd041126

Fang, M., Albrecht, B., Jung, E., Kollias, P., Jonsson, H., & PopStefanija, I. (2017). Retrieval of vertical air motion in precipitating clouds using Mie scattering and comparison with in situ measurements. *Journal of Applied Meteorology and Climatology*, *56*(3), 537–553. https://doi.org/10.1175/jamc-d-16-0158.1

Feingold, G., & Levin, Z. (1986). The lognormal fit to raindrop spectra from frontal convective clouds in Israel. *Journal of Climate and Applied Meteorology*, *25*(10), 1346–1363. https://doi.org/10.1175/1520-0450(1986)025<1346:tlftrs>2.0.co;2

Fletcher, J. K., Bretherton, C. S., Xiao, H., Sun, R., & Han, J. (2014). Improving subtropical boundary layer cloudiness in the 2011 NCEP GFS. *Geoscientific Model Development*, *7*(5), 2107–2120. https://doi.org/10.5194/gmd-7-2107-2014

Görsdorf, U., Lehmann, V., Bauer-Pfundstein, M., Peters, G., Vavriv, D., Vinogradov, V., & Volkov, V. (2015). A 35-GHz polarimetric Doppler radar for long-term observations of cloud parameters—Description of system and data processing. *Journal of Atmospheric and Oceanic Technology*, *32*(4), 675–690. https://doi.org/10.1175/jtech-d-14-00066.1

Jensen, J. B., Lee, S., Krummel, P. B., Katzfey, J., & Gogoasa, D. (2000). Precipitation in marine cumulus and stratocumulus.: Part I: Thermodynamic and dynamic observations of closed cell circulations and cumulus bands. *Atmospheric Research*, *54*(2–3), 117–155. https://doi.org/10.1016/s0169-8095(00)00040-5

Kalmus, P., & Lebsock, M. (2017). Correcting biased evaporation in CloudSat warm rain. *IEEE Transactions on Geoscience and Remote Sensing*, *55*(11), 6207–6217. https://doi.org/10.1109/tgrs.2017.2722469

Kirsch, B., Clemens, M., & Ament, F. (2019). Stratiform and convective radar reflectivity-rain rate relationships and their potential to improve radar rainfall estimates. *Journal of Applied Meteorology and Climatology*, *58*(10), 2259–2271. https://doi.org/10.1175/jamc-d-19-0077.1

Klingebiel, M., Ghate, V. P., Naumann, A. K., Ditas, F., Pöhlker, M. L., Pöhlker, C., et al. (2019). Remote sensing of sea salt aerosol below trade wind clouds. *Journal of the Atmospheric Sciences*, *76*(5), 1189–1202. https://doi.org/10.1175/jas-d-18-0139.1

Lawson, R. P., O'Connor, D., Zmarzly, P., Weaver, K., Baker, B., Mo, Q., & Jonsson, H. (2006). The 2D-S (stereo) probe: Design and preliminary tests of a new airborne, high-speed, high-resolution particle imaging probe. *Journal of Atmospheric and Oceanic Technology*, *23*(11), 1462–1477. https://doi.org/10.1175/jtech1927.1

Leon, D. C., Wang, Z., & Liu, D. (2008). Climatology of drizzle in marine boundary layer clouds based on 1 year of data from CloudSat and Cloud-Aerosol Lidar and Infrared Pathfinder Satellite Observations (CALIPSO). *Journal of Geophysical Research*, *113*(D8), D00A14. https://doi.org/10.1029/2008jd009835

Mätzler, C. (2002). MATLAB functions for Mie scattering and absorption, version 2.

Max Planck Institute for Meteorology. (2016). Barbados Cloud Observatory (BCO) radar, lidar, and surface meteorological observations [Dataset]. Retrieved from https://observations.mpimet.mpg.de/repository/entry/show?entryid=9c71b050-43f6-40cc-9424-627161c71ade

Medeiros, B., & Nuijens, L. (2016). Clouds at Barbados are representative of clouds across the trade wind regions in observations and climate models. *Proceedings of the National Academy of Sciences*, *113*(22), E3062–E3070. https://doi.org/10.1073/pnas.1521494113

Naumann, A. K., & Seifert, A. (2016). Recirculation and growth of raindrops in simulated shallow cumulus. *Journal of Advances in Modeling Earth Systems*, *8*(2), 520–537. https://doi.org/10.1002/2016ms000631

Niebaum. (2024). Constraining rain evaporation during the EUREC^{4}A campaign with the super-droplet-model CLEO. MS thesis. *Max Planck Institute for Meteorology, 1118884*.

O'Connor, E. J., Hogan, R. J., & Illingworth, A. J. (2005). Retrieving stratocumulus drizzle parameters using Doppler radar and lidar. *Journal of Applied Meteorology*, *44*(1), 14–27. https://doi.org/10.1175/jam-2181.1

Radtke, J., Vogel, R., Ament, F., & Naumann, A. K. (2023). Spatial organisation affects the pathway to precipitation in simulated trade-wind convection. *Geophysical Research Letters*, *50*(20), e2023GL103579. https://doi.org/10.1029/2023GL103579

Rapp, A. D., Lebsock, M., & L'Ecuyer, T. (2013). Low cloud precipitation climatology in the southeastern Pacific marine stratocumulus region using CloudSat. *Environmental Research Letters*, *8*(1), 014027. https://doi.org/10.1088/1748-9326/8/1/014027

Rosenfeld, D., & Mintz, Y. (1988). Evaporation of rain falling from convective clouds as derived from radar measurements. *Journal of Applied Meteorology and Climatology*, *27*(3), 209–215. https://doi.org/10.1175/1520-0450(1988)027<0209:eorffc>2.0.co;2

Sarkar, M., Bailey, A., Blossey, P., de Szoeke, S. P., Noone, D., et al. (2023a). Sub-cloud rain evaporation in the North Atlantic winter trade winds derived by pairing isotopic data with a bin-resolved microphysical model. *Atmospheric Chemistry and Physics*, *23*(19), 12671–12690. https://doi.org/10.5194/acp-23-12671-2023

Sarkar, M., Bailey, A., Blossey, P., de Szoeke, S. P., Noone, D., et al. (2023b). S23 bin-resolved Lagrangian rain evaporation model code [Software]. *Archived in supplementary information of: Sub-cloud rain evaporation in the North Atlantic winter trade winds derived by pairing isotopic data with a bin-resolved microphysical model. Atmospheric Chemistry and Physics*, *23*(19), 12671–12690. https://doi.org/10.5194/acp-23-12671-2023

Sarkar, M., Zuidema, P., Albrecht, B., Ghate, V., Jensen, J., Mohrmann, J., & Wood, R. (2020). Observations pertaining to precipitation within the Northeast Pacific stratocumulus-to-cumulus transition. *Monthly Weather Review*, *148*(3), 1251–1273. https://doi.org/10.1175/mwr-d-19-0235.1

Sarkar, M., Zuidema, P., & Ghate, V. (2021). Clarifying remotely retrieved precipitation of shallow marine clouds from the NSF/NCAR Gulfstream V. *Journal of Atmospheric and Oceanic Technology*, *38*(9), 1657–1670. https://doi.org/10.1175/jtech-d-20-0166.1

Seifert, A., & Heus, T. (2013). Large-eddy simulation of organized precipitating trade wind cumulus clouds. *Atmospheric Chemistry and Physics*, *13*(11), 5631–5645. https://doi.org/10.5194/acp-13-5631-2013

Snodgrass, E. R., Di Girolamo, L., & Rauber, R. M. (2009). Precipitation characteristics of trade wind clouds during RICO derived from radar, satellite, and aircraft measurements. *Journal of Applied Meteorology and Climatology*, *48*(3), 464–483. https://doi.org/10.1175/2008jamc1946.1

Srivastava, R. C. (1985). A simple model of evaporatively driven dowadraft: Application to microburst downdraft. *Journal of the Atmospheric Sciences*, *42*(10), 1004–1023. https://doi.org/10.1175/1520-0469(1985)042<1004:asmoed>2.0.co;2

Stevens, B. (2005). Atmospheric moist convection. *Annual Review of Earth and Planetary Sciences*, *33*(1), 605–643. https://doi.org/10.1146/annurev.earth.33.092203.122658

Stevens, B., Bony, S., Farrell, D., Ament, F., Blyth, A., Fairall, C., et al. (2021). EUREC 4 a. *Earth System Science Data Discussions*, *2021*(8), 1–78. https://doi.org/10.5194/essd-13-4067-2021

Stevens, B., Farrell, D., Hirsch, L., Jansen, F., Nuijens, L., Serikov, I., et al. (2016). The Barbados Cloud Observatory: Anchoring investigations of clouds and circulation on the edge of the ITCZ. *Bulletin of the American Meteorological Society*, *97*(5), 787–801. https://doi.org/10.1175/bams-d-14-00247.1

Stevens, B., Vali, G., Comstock, K., Wood, R., Van Zanten, M. C., Austin, P. H., et al. (2005). Pockets of open cells and drizzle in marine stratocumulus. *Bulletin of the American Meteorological Society*, *86*(1), 51–58. https://doi.org/10.1175/bams-86-1-51

Sundqvist, H., Berge, E., & Kristjánsson, J. E. (1989). Condensation and cloud parameterization studies with a mesoscale numerical weather prediction model. *Monthly Weather Review*, *117*(8), 1641–1657. https://doi.org/10.1175/1520-0493(1989)117<1641:cacpsw>2.0.co;2

Tompkins, A. M. (2001). Organization of tropical convection in low vertical wind shears: The role of cold pools. *Journal of the Atmospheric Sciences*, *58*(13), 1650–1672. https://doi.org/10.1175/1520-0469(2001)058<1650:ootcil>2.0.co;2

Torri, G., & Kuang, Z. (2016). Rain evaporation and moist patches in tropical boundary layers. *Geophysical Research Letters*, *43*(18), 9895–9902. https://doi.org/10.1002/2016gl070893

Van Zanten, M. C., Stevens, B., Vali, G., & Lenschow, D. H. (2005). Observations of drizzle in nocturnal marine stratocumulus. *Journal of the Atmospheric Sciences*, *62*(1), 88–106. https://doi.org/10.1175/jas-3355.1

Vogel, R., Konow, H., Schulz, H., & Zuidema, P. (2021). A climatology of trade-wind cumulus cold pools and their link to mesoscale cloud organization. *Atmospheric Chemistry and Physics*, *21*(21), 16609–16630. https://doi.org/10.5194/acp-21-16609-2021

Wood, R. (2005). Drizzle in stratiform boundary layer clouds. Part I: Vertical and horizontal structure. *Journal of the Atmospheric Sciences*, *62*(9), 3011–3033. https://doi.org/10.1175/jas3529.1

Worden, J., Noone, D., & Bowman, K. (2007). Importance of rain evaporation and continental convection in the tropical water cycle. *Nature*, *445*(7127), 528–532. https://doi.org/10.1038/nature05508

Zheng, X., Klein, S. A., Ghate, V. P., Santos, S., McGibbon, J., Caldwell, P., et al. (2020). Assessment of precipitating marine stratocumulus clouds in the E3SMv1 atmosphere model: A case study from the ARM MAGIC field campaign. *Monthly Weather Review*, *148*(8), 3341–3359. https://doi.org/10.1175/mwr-d-19-0349.1